Geomechanics and Engineering, *Vol. 39, No. 5 (2024) 441-453*
https://doi.org/10.12989/gae.2024.39.5.441

Spatial size effect study of broken-expansion mass using rock-like materials under the 110/N00 mining method

Pengfei Guo[1a], Yongxu Zhao[1], Xingyu Zhang*[2], Shiwei Deng[1],
Xiaoyun Zhang[1], Haijiang Zhang[1], Zhikang Li[1] and Manchao He[3]

[1]Key Laboratory of Rock Mechanics and Geohazards of Zhejiang Province, School of Civil Engineering,
Shaoxing University, Shaoxing 312000, China
[2]Faculty of Geo-Data Science, Geodesy and Environmental Engineering, AGH University of Science and Technology,
Krakow 30-059, Poland
[3]State Key Laboratory for Geomechanics and Deep Underground Engineering, China University of Mining and Technology,
Beijing 100083, China

(*Received March 10, 2024, Revised November 21, 2024, Accepted November 27, 2024*)

Abstract. The spatial size effect (SSE) of the broken-expansion mass is crucial in mining engineering, particularly with the promotion of the 110/N00 mining method. We analyzed the broken-expansion characteristics of bulking mass and introduced the space ratio and SSE coefficient to understand the SSE of broken-expansion mass. The results and analyses show a clear SSE in broken-expansion mass, and the suggested space ratio can be utilized to describe SSE. When the space ratio increases, the initial (K_I) and residual (K_R) broken-expansion factors increase, and the greater the space ratio, the more rapidly the increase. K_I generally determines K_R, but the compression inhibits SSE. The proposed SSE coefficient can express the SSE and the inhibition. Additionally, the SEE coefficient explains the SSE differentiation in the displacement characteristics. A larger space ratio leads to a greater volume reduction. Meanwhile, the bulking samples show a growing compressive capacity, and it can benefit from a smaller accumulation area. Compression failure in bulking mass is a dynamic process where structures change from loose to firm. The upper samples fail and fill voids, and the lower samples adjust positions to prevent failure. Finally, the discussion suggests the implications to the 110/N00 mining method.

Keywords: broken-expansion characteristic; bulking rock; compression tests; spatial size effect

1. Introduction

Broken-expansion characteristic of rock is a crucial property in underground excavation and mining (Moosavi and Ghadernejad 2021). For example, it is essential to consider the broken-expansion characteristic of rock in designing the support and understanding how the mine pressure distributes in underground mining (Bednarek *et al.* 2020, Guo *et al.* 2024, Yavuz 2004). Meanwhile, different mining and geological conditions can cause the spatial size effects of broken-expansion mass, including the size variations of the rock gravel and their accumulation area (Das 2000). The spatial size effect can further change the broken-expansion characteristics of rock mass (Fan and Liu 2017, Genis *et al.* 2018). In recent years, a novel non-pillar mining technology with automatically formed entry of 110/N00 mining method prevails in China (He *et al.* 2021, Zhang *et al.* 2020a), in which the broken-expansion mass plays a vital role in relieving the mining pressure (Zhang *et al.* 2020b, Zhang *et al.* 2023, Fu *et al.* 2024). Therefore, whether it is from the mining basics or the engineering development, understanding the characteristics of broken-expansion mass and its spatial size effect (SSE) is crucial in underground excavation and mining engineering.

Some scholars have studied the broken-expansion characteristics of rock through laboratory tests, numerical simulations, or field tests. Ma *et al.* (2019) tested the crushing behavior and seepage properties of bulking rock gangue under compression. They examined how particle size distribution and water content impact the crushing behavior and seepage properties of the bulking rock gangues. Guo *et al.* (2019) conducted a series of creep compaction tests on crushed mudstones with different grain compositions, and they discussed the influencing factors on the compaction creep behavior of the bulking crushed mudstone. Meng *et al.* (2021) used a particle discrete element method to simulate the time effect of the bulking coefficient of the broken rock under triaxial compression, and they analyzed how the axial and confining pressure influenced the bulking coefficient and the deformation characteristic. Li *et al.* (2021) used the particle flow simulation to conduct a study on the bulking rock and analyzed the deformation and evolution of crushed gangue when subjected to triaxial compression. Liu *et al.* (2021, 2022b) conducted experiments on the bearing characteristics of bulking gangue, and they investigated the relationship between the lumpiness, bulking factor, and supporting force of gangue. The existing research has

---

∗Corresponding author, Ph.D.
E-mail: zhangxy.leeh@outlook.com
[a]Associate Professor
E-mail: gpf2018@usx.edu.cn

ISSN: 2005-307X (Print), 2092-6219 (Online)

extensively reported the compaction characteristics and behavior of bulking rock. As the 110/N00 mining method is widely applied in the underground mining, a series of study regarding the broken-expansion mass is sparked. Wang *et al.* (2021) examined the compression behavior of crushed mudstones of varying particle sizes based on the scenario of 110 mining method. The study found that particle size significantly affects the deformation and lateral stress exerted on support structures, and the case of larger particles shows better deformation resistance and stability under pressure. Zhang *et al.* (2019) emphasized the positive effect of broken-expansion mass after the roof presplitting and mining. This approach allows the caved gangue to form a natural rib and support structure for stabilizing the gob-side entry and reducing mining pressure. However, the existing study lacks the fundamental research about the broken-expansion mass in the context of 110/N00 mining method. Meanwhile, few studies focus on the SSE of the broken-expansion rock mass. The size effect of rock has been a challenging topic in rock mechanics and engineering (Fakhimi and Tarokh 2013, Haeri *et al.* 2017, Haftani *et al.* 2014). This effect is no exception for broken-expansion rock mass. Apart from the sample size, the accumulation area probably has an influence. The accumulation area is a necessary consideration because of the different mining areas in practice (Fairhurst 2017, Wang 2014).

Nowadays, the provability of rock-like materials facilitates the research of experimental rock mechanics because it allows for the controlled replication of rock properties and the predefined configuration of practical scenarios (Gell *et al.* 2019, Pour *et al.* 2022). For example, Chang *et al.* (2019) used the artificial rock-like material of gypsum to investigate the strength anisotropy of rocks with crossing joints, and they found that joint orientation significantly influences the anisotropic strength of the rock, with critical failure patterns closely associated with joint intersection angles. Yang *et al.* (2021) conducted a model experimental study about rock blasting by using the rock-like materials of gypsum to simulate the rock and to investigate the effects of in situ stresses on pre-splitting blasting damage and strain development, and they found that higher in situ stresses intensified blasting-induced damage and strain accumulation, with stress orientation significantly influencing fracture propagation patterns. Lee *et al.* (2023) adopted the rock-like materials of concrete with varying uniaxial compressive strength to investigate the performance of a full-scale TBM during excavation and illustrated the influence of material strength on TBM efficiency and wear interacting with the excavated rock. Moghaddam and Golshani (2024) conducted an experimental study using the rock-like material of concrete to investigate fracture propagation in the anisotropic rock under cyclic hydraulic fracturing. They found that cyclic injection reduced the breakdown pressure compared to monotonic injection and generated more complex fracture networks, which demonstrates the potential of hydraulic fatigue to improve reservoir stimulation. The use of rock-like materials in experimental rock mechanics allows for a systematic study of mechanical behaviors, fracture mechanisms, and the effects of specific parameters under various conditions that are challenging to replicate with natural rock samples.

To fundamentally understand the spatial size effect of broken-expansion rock, this work conducts the experimental study using rock-like materials and then explores the broken-expansion characteristics of rock and its SSE concerning the 110/N00 mining method. We propose the relevant parameters of SSE and then conduct multiple compression tests on the bulking samples, as well as considering different sample sizes and accumulation areas. Based on the test results, we discuss the SSE on the broken-expansion factors, compression displacement, and mechanical failure characteristics. The findings are expected to enhance understanding of the broken-expansion characteristics and its SSE, which can help optimize the application of the 110/N00 mining method.

2. Spatial size effect (SSE) of broken-expansion mass in different mining methods

The roof strata above the coal seam would break and cave during mining. Generally, three zones are formed in the traditional mining method. According to the strata characteristics, the three zones are the caving zone, fractured zone, and sagging zone. As shown in Fig. 1(a), the immediate roof directly collapses after mining. The formed bulking rock naturally piles up in the gob, causing its volume to expand. As the strata collapse, the main roof slides and rotates, and the overlying strata bend and subside. The broken rock mass is compressed in the caving zone.

The 110/N00 mining method cleverly uses the broken-expansion characteristics of rock mass to achieve the balanced underground mining. The broken-expansion mass plays a vital role in mitigating the mining pressure to ensure the safety of the automatically formed roadway. As shown in Fig. 1(b), the height of the caving zone increases under the roof-cutting effect. The caved rock mass fills the gob, and the broken-expansion mass provides the natural support to resist the overburden movement. The strata movement becomes moderate after mining compared to the situation in the traditional mining method (Zhang *et al.* 2020a).

The bulking mass resembles the granular material. The accumulation height can exceed the initial thickness of the overlying rock deposited. This expansion characteristics can be expressed by the broken-expansion factor K

$$K = \frac{V}{V_{\mathrm{O}}} \approx \frac{H}{H_{\mathrm{O}}} \tag{1}$$

where V is the accumulation volume of the collapsed rock mass; V_{O} is the original deposition volume of the immediate roof; H is the accumulation height of the collapsed rock mass; and H_{O} is the original deposition height of the immediate roof.

Two states always exist whether in the traditional or 110/N00 mining method because the broken-expansion factor changes under the compression resulting from the strata movement. Initially, the roof falls in the gob where

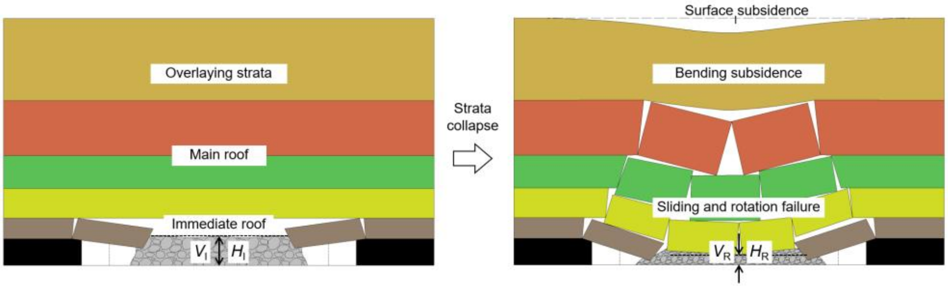

(a) Traditional mining method

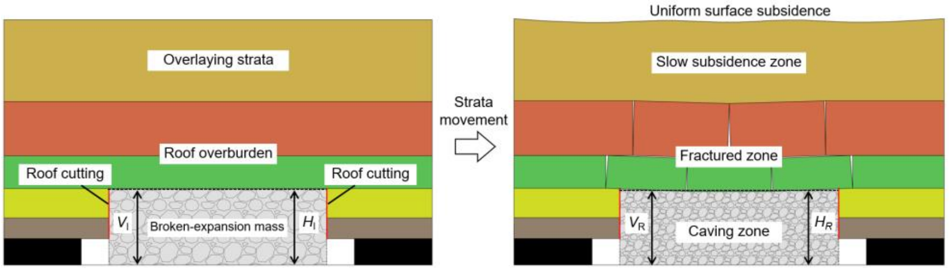

(b) 110/N00 mining method

Fig. 1 Schematic diagram of broken-expansion characteristics of rock mass during strata movement

rock blocks pile up disorderly. The accumulated rock mass naturally stays without the top pressure. Afterward, the rock mass in the caving zone is compressed with the strata movement, so the broken-expansion factor decreases. However, the factor can still be greater than 1 because the pressure cannot be infinite, so the rock mass is impossible to be compressed to the original height. Therefore, there are two factors corresponding to the initial and final states, i.e., the initial broken-expansion factor K_{I} and the residual broken-expansion factor K_{R}

$$\begin{cases} K_{\mathrm{I}} = \dfrac{V_{\mathrm{I}}}{V_{\mathrm{O}}} \approx \dfrac{H_{\mathrm{I}}}{H_{\mathrm{O}}} \\ K_{\mathrm{R}} = \dfrac{V_{\mathrm{R}}}{V_{\mathrm{O}}} \approx \dfrac{H_{\mathrm{R}}}{H_{\mathrm{O}}} \end{cases} \tag{2}$$

where V_{I} and V_{R} are the initial and residual accumulation volume of the collapse rock mass; V_{O} is the original deposition volume of the immediate roof; H_{I} and H_{R} are the initial and residual accumulation height of the collapse rock mass; and H_{O} is the original deposition height of the immediate roof.

However, there are differences in the gob-roof fracture between the two mining methods. The working face experiences periodic mining pressure, and the roof breaks successively while the roof fractures upon reaching its limit span. As shown in Fig. 2, the fractured strata can be considered as rock blocks with equal periodic lengths and the boundaries of fracture. In traditional mining, the gob roof typically fractures in an "O-X" pattern, as shown in Fig. 2(a). However, roof cutting is implemented along with the automatically formed roadway in the 110/N00 mining method (Fig. 2(b)). This case causes approximately regular square fractures within the roof, as verified by Liu *et al*. (2022a).

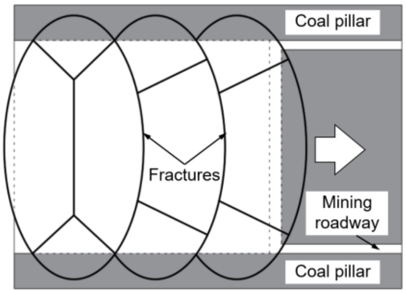

(a) Traditional mining method

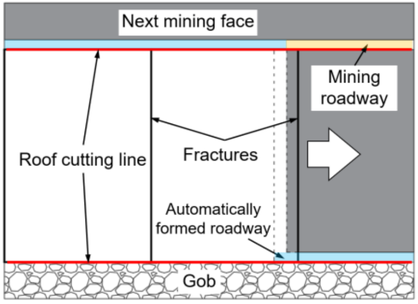

(b) 110/N00 mining method

Fig. 2 Schematic diagram of roof fracture characteristics of gob in different mining methods

Additionally, the broken-expansion factors of K_{I} and K_{R} differ from different mining geological conditions. The conditions determine the direct variables influencing the broken-expansion factor, such as the rock block size and filling space. The mining area, i.e., filling space, is particular for a specific site. When the rock block size changes, the ratio between the block size and the space length will change accordingly. This inevitably leads to a change in the filling density, so the broken-expansion factor changes. The 110/N00 mining method puts more emphasis on the role of broken-expansion characteristics of rock mass compared to the traditional one. For simplicity and

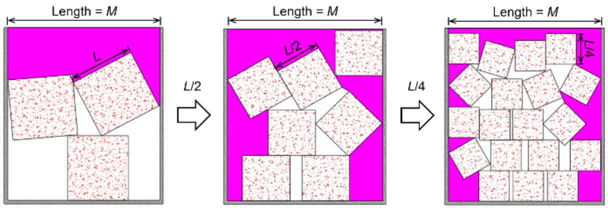

Fig. 3 Schematic diagram of spatial size effect of rock

excluding other influencing factors in the context of 110/N00 mining method, we assume square rock blocks randomly fill in a container while considering the roof fracture features in the 110/N00 mining method. As shown in Fig. 3, the length of filling space is *M*. When the rock block size decreases, the space occupied by the accumulated rock blocks clearly changes. Therefore, the occurrence of SSE is associated with changes in rock block size. Similarly, when the filling space length *M* changes, there also is SSE.

To quantify the influence of SSE, we define the space ratio *S* determined by the space length *M* and the side length *L*. The space ratio *S* can be expressed as

$$S=\frac{L}{M} \tag{3}$$

The space ratio *S* is influenced by the accumulation area and the rock block size. Therefore, in the three-dimensional space, the length *M* should be the minimum for the accumulation area, and the side length *L* should be the greatest for the rock block. Meanwhile, it suggests that smaller area lengths and larger rock block sizes lead to a more pronounced spatial ratio, therefore causing SSE. However, the space ratio *S* is a static index that reflects only the initial state of the accumulated rock. To better characterize the SSE of broken-expansion rock mass, we propose the SSE coefficient *C* which is defined as

$$C=\frac{\Delta K}{\Delta S} \tag{4}$$

where ΔK is the difference of broken-expansion factors as the space ratio *S* changes gradually, and ΔS is the corresponding difference in the space ratio. The SSE coefficient *C* captures variations in the broken-expansion factor driven by changes in the space ratio. As a dynamic parameter, the coefficient *C* accounts for both the broken-expansion effect and the influence of the space ratio. Consequently, the SSE effect of broken-expansion rock under varying space ratios can be effectively quantified using the SSE coefficient.

3. Laboratory experiment

3.1 Material preparation

Rock-like materials are widely used in rock mechanics tests because of their ease of use and controllability.

Table 1 Parameters of gypsum samples with different water-plaster ratios

Water–plaster ratio	Compressive strength /MPa	Tensile strength /MPa	Elastic modulus /MPa	Poisson's ratio
0.6	2.42	0.23	0.86	0.25
0.8	1.80	0.15	0.67	0.23
1.0	0.86	0.05	0.55	0.27

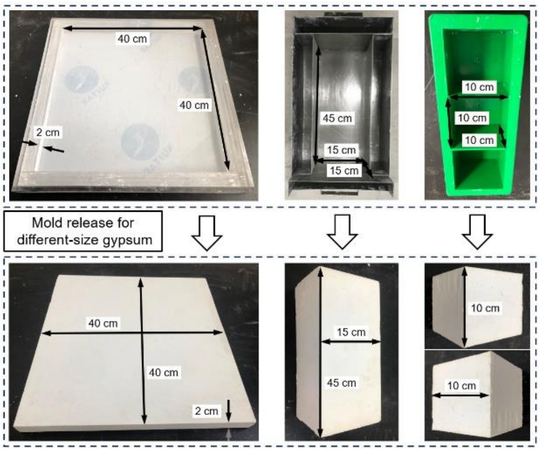

Fig. 4 Different-size molds and molded gypsum

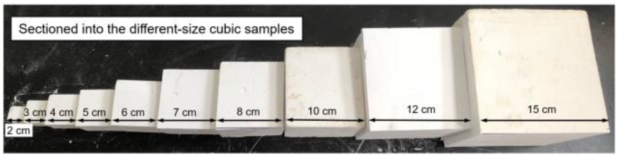

Fig. 5 Samples with different sizes

According to the test conditions and the documented research, we selected the rock-like material of gypsum to simulate rock to explore the broken-expansion characteristics of rock and its SSE. The uniform composition and availability of gypsum in controlled experimental conditions allow for consistent and reproducible results. Some research has demonstrated that gypsum can show similar properties to rock as long as using the proper ratios of water to plaster (Chang *et al*. 2019, Discenza *et al*. 2020, Yang *et al*. 2021), by which the gypsum is well-suited to simulating the brittle rock material (Sarfarazi *et al*. 2021). Therefore, we first tested the mechanical properties of high-strength gypsum with different ratios of water to plaster and obtained the parameters, as listed in Table 1.

According to the preliminary test results, the gypsum had the peak strength therein while at a water-plaster ratio of 0.6, so the samples were prepared with the ratio of 0.6:1. We then maintained the prepared gypsum at 25°C for 28 days so that the gypsum can achieve the ideal mechanical properties. As shown in Fig. 4, we employed different-size molds to prepare the samples with varying lengths. Finally, different-size cubic samples were sectioned, as shown in Fig. 5.

Table 2 Experimental parameters of group A (M = 30 cm)

Sample	A1	A2	A3	A4	A5	A6	A7	A8	A9	A10
Size (L)/cm	2	3	4	5	6	7	8	10	12	15
Space ratio (S)	0.067	0.100	0.133	0.167	0.200	0.233	0.267	0.333	0.400	0.500
Total fill mass /kg	3	3	3	3	3	3	3	3	3	3

Table 3 Experimental parameters of group B (M = 20 cm)

Sample	B1	B2	B3	B4	B5	B6	B7	B8	B9	B10
Size (L)/cm	2	3	4	5	6	7	8	10	12	15
Space ratio (S)	0.1	0.15	0.2	0.25	0.3	0.35	0.4	0.5	0.6	0.75
Total fill mass /kg	3	3	3	3	3	3	3	3	3	3

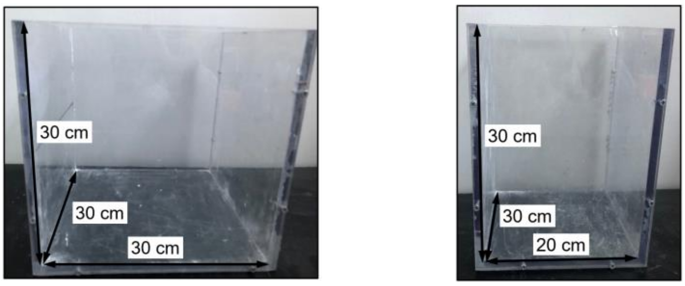

(a) The larger one (b) The smaller one

Fig. 6 Two containers with different accumulation areas

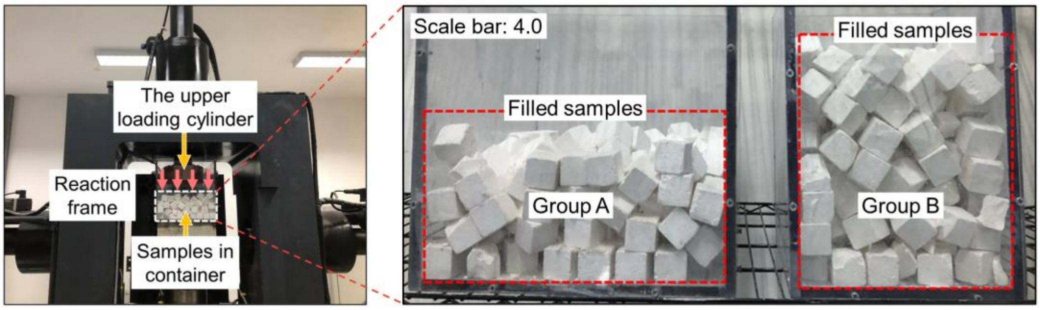

Fig. 7 Test setup and apparatus

3.2 Test scheme and equipment

According to the definition of the space ratio S, the broken-expansion characteristics of rock relate to not only the rock block size but also the accumulation area. Therefore, we additionally designed the two containers with different accumulation areas based on the different-size samples. As shown in Fig. 6, the containers were made of transparent polycarbonate. One is characterized by dimensions of 30 cm × 30 cm × 30 cm (M = 30 cm), and the other is 20 cm × 30 cm × 30 cm (M = 20 cm) for comparison.

Therefore, two groups of A and B, each with ten samples varying sizes, are established using two containers. Group A has a larger area than Group B. Tables 2 and 3 listed the experimental parameters of groups A and B. The space ratios are calculated separately, and the total fill mass is set as the same according to the mass conservation law.

Throughout the experiment, the indoor temperature was maintained at 26°C, and the relative humidity was stabilized at approximately 45%.

To ensure the test reproducibility and result reliability, the tests for both groups were repeated three times under identical conditions, with the average values serving as the final results. Abnormal data were validated through duplicate testing.

Fig. 7 shows an example of actual scenes when the 3-cm length samples were filled in. In this experiment, we dropped the samples freely from the same height to simulate the real situation. The initial accumulation height of the bulking samples was first measured. Then, the bulking samples in the container were pressured using the DRTB-1000 pressure test system. DRTB-1000 is a self-developed triaxial stress test system, and the axial pressure function is used in the test. The compaction was done by moving the upper loading cylinder downward, and the load

Table 4 Initial broken-expansion factors of K_I

Size (L)/cm	2	3	4	5	6	7	8	10	12	15
Group A	2.1	2.17	2.25	2.31	2.35	2.67	3.23	4.04	4.7	5.81
Group B	2.17	2.25	2.36	2.75	3.4	3.58	3.76	4.23	4.68	5.05

was applied at a stress rate of 1 MPa/min. The loading was kept for 150 s until the peak value reached 2.5 MPa. Each test was repeated three times for every size sample in the two groups, so the average value was taken as the result.

4. Results and analysis

4.1 Spatial size effect of initial broken-expansion characteristics

Table 4 presents the initial broken-expansion factors for groups A and B. There is a positive correlation between sample size and initial factors. As the sample size increased, the initial broken-expansion factor K_I increased as well. This phenomenon lies in not only the increased size of samples but also the interstitial space due to the random accumulation of samples.

Fig. 8 shows the variation curves of K_I with the change in size and space ratio. First, as shown in Fig. 8(a), although K_I both increased with an increase in size, there were differences in the upward trends between groups A and B. When the size increased to 4 cm in group A, K_I rose clearly but slew down at 6 cm. In group B, K_I did not clearly rise until the size reached 6 cm and then increased obviously. Therefore, there was an intersection between groups A and B at the 12 cm—position I. As the sample size changed, the accumulation area obviously influenced the K_I. When the sample size was less than 12 cm, a smaller accumulation area led to a bigger K_I. On the other hand, when the sample size was greater than 12 cm, a larger accumulation area resulted in a bigger K_I. However, there was not a clear rule for describing the change. If the independent variable of the size is changed into the space ratio, the curves are shown in Fig. 8(b). When the space ratio was less than 0.2, i.e., position II, the two curves were close. As the ratio increased, the K_I began to differentiate from each other, and the difference was enlarged, especially starting from the space ratio of 0.3. Therefore, the space ratio clearly influenced K_I. This influence was comparatively weak when the space ratio was less than 0.2. When the space ratio was greater than 0.2, K_I increased obviously as the space ratio increased. At the same time, the larger accumulation area (group A) led to a more evident increase effect than the smaller area (group B).

Based on the above results, we explored the impact of spatial size on K_I using the defined SSE coefficient C (Eq. 4). As shown in Fig. 9, the SSE coefficient C_I for the initial broken-expansion characteristic was the dependent variable, and it integrates the changes of broken-expansion effect and space ratio. The size change was the independent variable.

The curve graph therefore synthesized the relation of the three parameters. The two curves increased and then declined, illustrating the SSE variation trend while the sample size increased. The SSE was distinct when the sample size varied in the large size (6–15 cm in group A and 4–12 cm in group B). Nevertheless, the accumulation area still led to different responses. As the size was changed to the large, a smaller accumulation area, i.e. group B, earlier started to show a distinct SSE compared to group A. However, with an increased sample size, the SSE of Group A became stronger than that of Group B. Overall, the average SSE coefficient of Group A was 7.43, bigger than the 4.83 of Group B. According to these analyses, we can easily understand why there is an intersection in Fig. 8(a) when the sample size changed to the large, as well as the differentiation phenomenon in Fig. 8(b) when the space ratio increased.

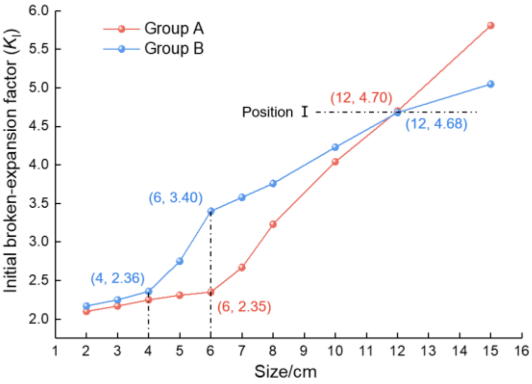

(a) Size

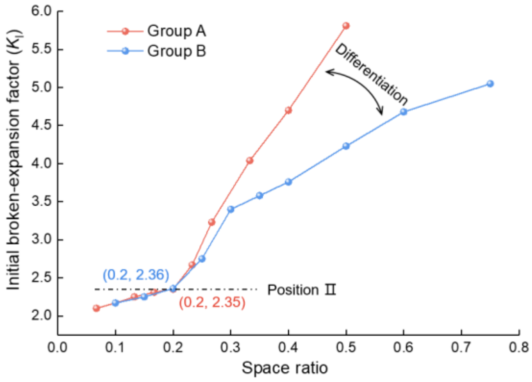

(b) Space ratio

Fig. 8 Variation of the initial broken-expansion factor with the size and space ratio changes

4.2 Spatial size effect of residual broken-expansion characteristics

The residual broken-expansion factor K_R is the other crucial characteristic of broken-rock mass in underground mining. After examining the initial factor K_I, we examined

Table 5 Residual broken-expansion factors K_R

Size (L)/cm	2	3	4	5	6	7	8	10	12	15
Group A	1.18	1.22	1.26	1.3	1.34	1.67	1.89	2.56	2.8	3.13
Group B	1.21	1.28	1.34	1.73	2.21	2.34	2.45	2.6	2.76	2.93

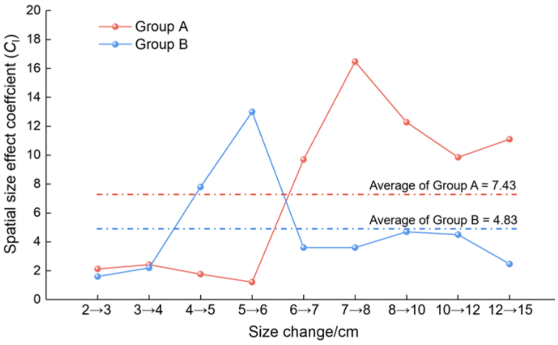

Fig. 9 The variation of C_I while changing the sample size

the residual factor K_R by compacting the broken-expansion rock mass according to the test scheme. Table 5 shows the residual broken-expansion factors for the different sample sizes of groups A and B. Compared to the initial factors K_I, the residual factors K_R would decrease after the compression. Similarly, the factors K_R increased as the sample sizes increased, which is identical to the general variation trend of K_I.

Fig. 10(a) shows the variation curve of the residual broken-expansion factor K_R when the sample size increased. Compared to K_I, K_R presented a similar trend. Whether in groups A or B, their initiation points for rapid growth did not change, and the values of K_R are close and even the same, with a value of 1.34 in this case. Meanwhile, the increase of K_R in group B also slew down at the size of 6 cm, so there was also an intersection in the latter half of the curves. While observing the variation curve of K_R with the change of the space ratio (Fig. 10(b)), we can still find a similar overall trend to that of K_I. Whether in groups A or B, they rapidly increased starting from the space ratio of 0.2, and a differentiation emerged in the second half. Therefore, K_I generally determines K_R in terms of the SSE. However, some changes should be noteworthy. In Fig. 10(a), the intersection, i.e. position III, moved forward to the range of the 10–12 cm compared to that in Fig. 8(a), i.e. position I. In Fig. 10(b), the differentiation between the curves of groups A and B narrowed compared to that in Fig. 8(b). For example, at the space ratio of 0.5, the difference value was 0.53 for K_R and less than 1.58 for K_I. Furthermore, the starting point of differentiation for K_R moved farther than that for K_I, i.e., the position V was relative to the position II. This series of differences illustrates that the compression inhibited SSE.

The SSE coefficient C can intuitively explain the inhibition effect. Fig. 11(a) shows the variation of C_R as the sample size gradually changed. The overall variation was similar to that of C_I (Fig. 9), presenting a trend of increasing and then decreasing. However, the variation amplitude shrunk, especially for group A. The average value of group A was reduced by 42.7% from 7.43 of C_I to 4.26 of C_R, and the average value of group B decreased by 33.1% from 7.43 of C_I to 4.26 of C_R. Fig. 11(b) summarizes the

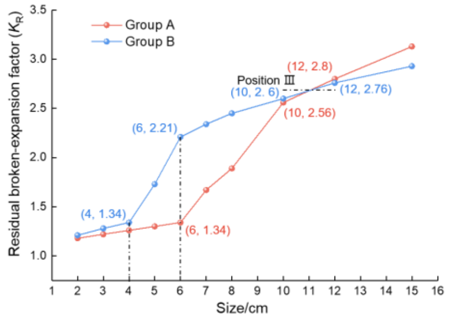

(a) Size

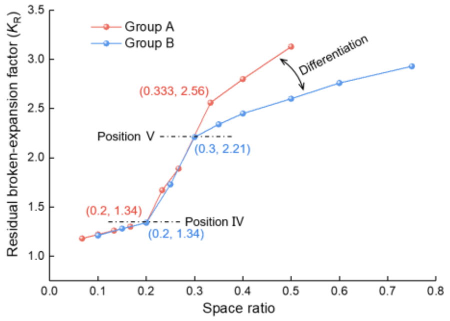

(b) Space ratio

Fig. 10 Variation of the residual broken-expansion factor with the size and space ratio changes

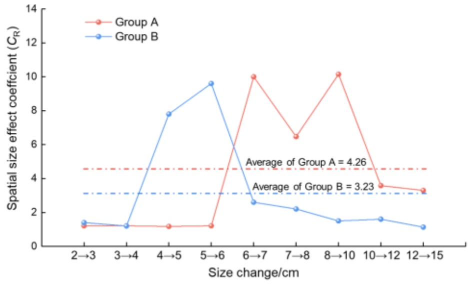

(a) C_R

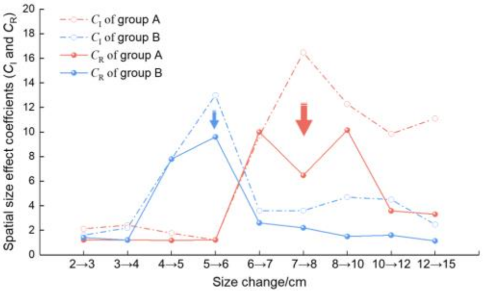

(b) C_I and C_R

Fig. 11 The variations of SSE coefficients as the sample size gradually changed

Table 6 Summary test results of group A

Size/cm Indexes	2	3	4	5	6	7	8	10	12	15
S	0.067	0.1	0.133	0.167	0.2	0.233	0.267	0.333	0.4	0.5
K_{I}	2.1	2.17	2.25	2.31	2.35	2.67	3.23	4.04	4.7	5.81
K_{R}	1.18	1.22	1.26	1.3	1.34	1.67	1.89	2.56	2.8	3.13
V/%	43.8	43.8	44	43.7	43	37.5	41.5	36.6	40.4	46.1
H_{I}/mm	80	82	85	88	89	101	122	153	178	220
H_{R}/mm	45	46	48	50	51	63	72	97	106	119
D/mm	35	36	37	38	38	38	50	56	72	101

Table 7 Summary test results of group B

Size/cm Indexes	2	3	4	5	6	7	8	10	12	15
S	0.1	0.15	0.2	0.25	0.3	0.35	0.4	0.5	0.6	0.75
K_{I}	2.17	2.25	2.36	2.75	3.4	3.58	3.76	4.23	4.68	5.05
K_{R}	1.21	1.28	1.34	1.73	2.21	2.34	2.45	2.55	2.8	2.93
V/%	44.2	43.1	43.2	37.1	35	34.6	34.8	38.5	41	42
H_{I}/mm	123	128	134	156	193	203	214	240	266	287
H_{R}/mm	69	73	76	98	126	133	139	145	159	167
D/mm	54	55	58	58	67	70	75	95	107	120

variations of C_{I} and C_{R} for groups A and B. Whether in groups A or B, the SSE coefficients mostly reduced from C_{I} to C_{R}. The reduction in group A was more significant than that in group B. The most considerable decrease in group A occurred when the sample size changed from 7 to 8 cm, and the reduction value was 10. In group B, the greatest reduction occurred when the sample size changed from 5 to 6 cm, and the reduction value was 3.4. Meanwhile, this reduction was not apparent in the small size of the sample (2–5 in group B and 2–7 in group A), mainly due to the subtle SSE. Therefore, the inhibition to SSE was more evident in the case with a more extensive accumulation area, and this inhibition would be amplified when the sample size was large.

4.3 Compaction characteristics of broken-expansion rock mass

Tables 6 and 7 separately summarize the test results of groups A and B. S is the space ratio (Eq. (3)). V denotes the change rate between K_{I} and K_{R}, and it is calculated via $\frac{K_{\mathrm{I}}-K_{\mathrm{R}}}{K_{\mathrm{I}}}\times 100\%$. D is the displacement when the samples were compacted, and it is calculated from $H_{\mathrm{I}}-H_{\mathrm{R}}$. As the sample size increased, the variation trend of V showed an increase followed by a decline. This phenomenon corresponds to the previous analysis—because of the change in SSE coefficient C. It is noteworthy that D generally increased with the evolution of the sample size, which illustrates that the individual compaction differed with regard to SEE.

Fig. 12 presents the stress-displacement curves of groups A and B about the ten individual tests. The curves help understand the compaction process of samples when the loading increases. Curves are differentiated regarding the different sample sizes. For group A (Fig. 12(a)), the displacement curves were close when the sample size was 2–7 cm. If the size continued to change to 8 cm, the curve differentiation was apparent. This situation can be explained by the SSE coefficients of C_{I} and C_{R}, in which the difference between C_{I} and C_{R} was significant compared to the others—referring to Fig. 11(b). For group B, the curves of 2–5 cm were close. When the size changed to 6 cm, the differentiation clearly existed. Similarly, the difference between C_{I} and C_{R} at 5–6 cm for group B was larger than the others. Meanwhile, an apparent differentiation also existed from 8 to 10 cm in group B. Although the difference between C_{I} and C_{R} was not as large as the case of 5–6 cm, the change of the space ratio contributes too. The change of the space ratio for 8–10 cm was greater than that for 5–6 cm. Eq. (5) helps the understanding, and it can be derived from Eqs. (2) and (4).

$$\Delta D = H_{0}\Delta S(C_{\mathrm{I}} - C_{\mathrm{R}}) \tag{5}$$

where ΔD is the displacement difference. The product of $C_{\mathrm{I}}-C_{\mathrm{R}}$ and ΔS matters. Combined with Fig. 11 (b), we can quickly grasp the reasons for the curve differentiations. Given an exact change in the space ratio, the C_{I} and C_{R} difference decides the compaction displacement's SSE. Therefore, the coefficient C expresses well on the SSE.

Observing the curves, we can identify three stages: rapid compaction, slow compaction, and compacted stabilization. The rapid compaction occurs first because of ample space among the samples that can be compressed quickly under the

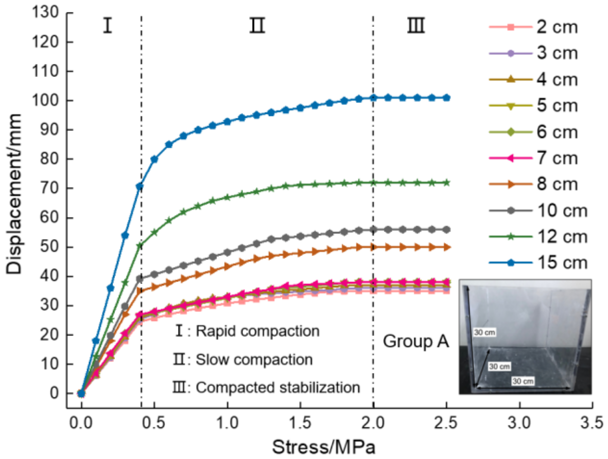

(a) Group A

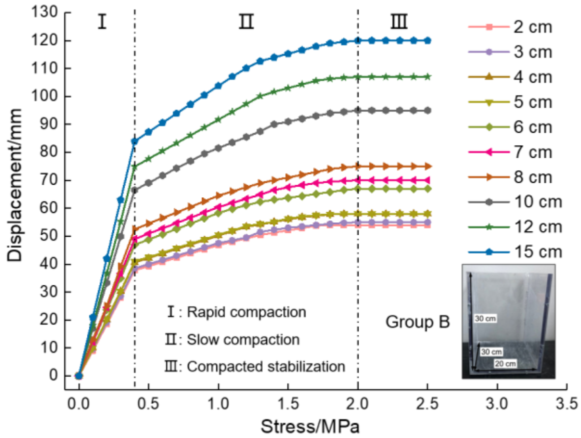

(b) Group B

Fig. 12 Stress-displacement curves of groups A and B

pressure. The displacement in stage I accounted for around 70% of the total. Then the slow compaction follows, in which the space had been contracted. Interestingly, regardless of sample sizes or groups, all curves entered stage II at 0.4 MPa, about one-sixth of the material's compressive strength. In the stage II, the displacement accounted for 30% of the total displacement. All curves approximately ended at 2.0 MPa, which is around five-sixths of the material's compressive strength. Finally, the compacted stabilization (stage III came when the bulking samples reached a new equilibrium, and the displacement no longer increased obviously, though the loading became greater. Compared with the curves in a certain group, the larger sample size resulted in a greater displacement, indicating that a greater spatial ratio leads to a more substantial volume reduction. Correspondingly, the curves for large-size samples are steeper than the other curves.

If comparing with the curves of the same sample size but in different groups, we found a larger compression displacement in group B than in group A. While comparing groups A and B with the same block size, group A had a smaller space ratio than group B, i.e., $S_A<S_B$. A larger space ratio leads to more vertical space formed among the samples, so compressible space increased in the rapid compression stage of group B. Judging from the horizontal comparisons, we acknowledged that, in stage I, the displacement for all curves in group B was correspondingly greater than those in group A.

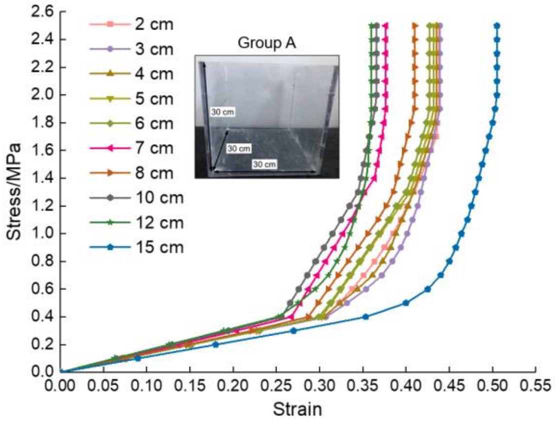

(a) Group A

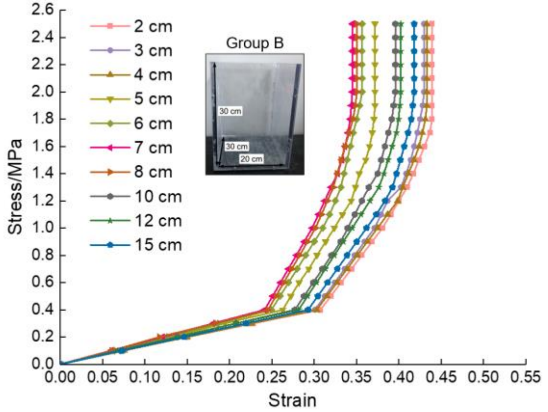

(b) Group B

Fig. 13 Stress-strain curves of groups A and B

4.4 Mechanical and failure characteristics of broken-expansion rock mass

To further study the mechanical characteristics of broken-expansion rock mass and its SSE during the loading, we obtained the stress-strain curves of groups A and B, as shown in Fig. 13. As the strain increased, the stresses of all curves increased linearly and then rose exponentially. The linear increase segment corresponded to stage I of the rapid compaction (Fig. 12), where the bulking samples were loosely stacked to be compacted. The exponentially increase segment included the stages II and III, where the bulking samples were closely contacted. The results indicate that the broken-expansion rock mass has a growing ability to withstand compression. This compressive capacity would be clearly strengthened after going through a relatively slow linear increase. According to the test results, the turning position is located in the strain between 0.24 and 0.35. In addition, the mechanical characteristics showed SSE whether in the different sample sizes of a group or the same size sample in different groups. First, in a specific accumulation area, i.e., a certain group in the test, the curve differentiations did not show a definite rule with the sample size change. For group A, the 12-cm sample first entered the exponential increase segment while the 15-cm sample was the last. For group B, the 7-cm sample first entered the exponential increase segment while the 2-cm sample was the last. Therefore, the sample size can affect the duration when the bulking rock rebalances, but there is no

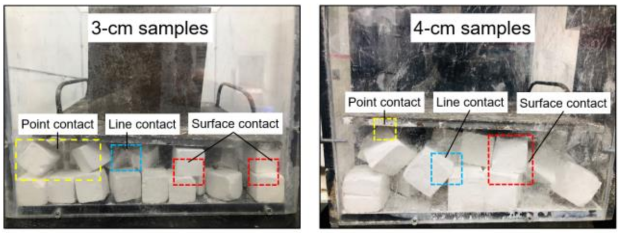

(a) Initial state

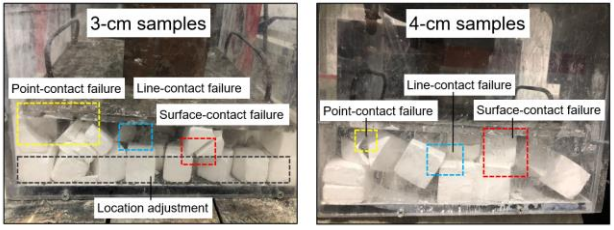

(b) Loaded state

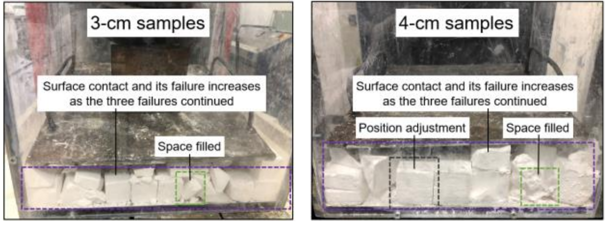

(c) Compacted stabilization state

Fig. 14 Dynamical characteristics of bulking samples under the loading

regular correlation between them. If comparing the curves in two groups, we can discover that the curve differentiation of group B was smaller than that of group A. The turning position in group B was located in the strain between 0.24–0.31, while the strain was between 0.25–0.35 in group A. Overall, the comparison illustrates that a smaller accumulation area is more beneficial to the increase of compressive capacity or the rebalance of the broken-expansion rock mass under compression.

The curve trend of stress-strain is closely related to the dynamic characteristics of bulking samples during the compression. Fig. 14 shows the examples and the scenes in different states when the bulking samples were compressed. As shown in Fig. 14(a), the samples were randomly stacked in the initial state. Three contact forms were identified, including the point, line, and surface contact. When the samples in the initial state were loaded, the block failure and the self-adjustment occurred. As shown in Fig. 14(b), the upper samples were compressed to fail, and the lower samples spontaneously adjusted their positions to prevent the failure. The point-contact failure was the most severe, and the sample was broken into smaller blocks and pieces. Line-contact and surface-contact failures were moderate, with several penetrated cracks at most. This stage corresponded to the linear increase segment of the stress-strain curve. The failure and adjustment made the bulking samples compact, and a higher-strength structure formed. As shown in Fig. 14(c), since the samples adjusted their positions and the broken parts filled the space, the structure was characterized by more surface contacts among samples.

Table 8 Physicomechanical parameters of tested limestone

Density (g/cm^3)	Compressive strength (MPa)	Elastic modulus (MPa)	Poisson's ratio
2.26	13.5	19.7×10^3	0.2

(a) Experimental container

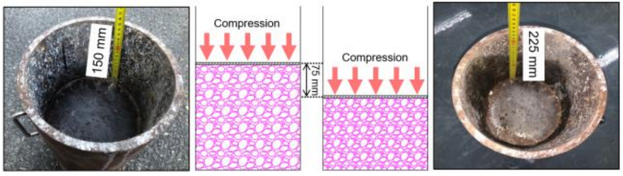

(b) Experiment scenes

Fig. 15 Experiment design and materials

The structure became firmer than before, and the stage corresponded to the exponential increase segment of the stress-strain curve.

Therefore, the compression failure of the bulking samples was a dynamic transformation. The point and line contacts were transformed into the surface contacts, and the structure was transformed from loose into firm. During this course, the upper samples failed and filled into the void, and the lower samples spontaneously adjusted their positions to prevent the failure. Finally, the bulking samples were compacted to a high-strength body resistant to compression.

5. Discussion

5.1 Calibration

To calibrate the tested results and their practical meaning, we selected the limestone with a 3–4 cm grain size to replicate the compression experiment. The basic parameters of the limestone are listed in Table 8. The container was a cylindrical structure made of 45# steel. As shown in Fig. 15(a), the cylinder had a diameter of 20 cm and a height of 40 cm. The top cover was 10 mm thick with a diameter of 19 cm.

A total of 9-kg limestone gravel was added to the container, and the top cover was placed on the gravel. We then placed the container in the loading machine of DRTB-1000 test apparatus. The loading rate was 0.5 MPa/min, and the maximum pressure reached 13.5 MPa. The pressure was not kept until the vertical displacement changed less than 0.1 mm within 30 s. At this moment, the compressed gravel was considered as in a stable state. As shown in Fig. 15(b), the top space height was changed from 150 mm to 225 mm after the test. The bulking limestone was compressed from the initial height of 240 mm to the final height of 165 mm.

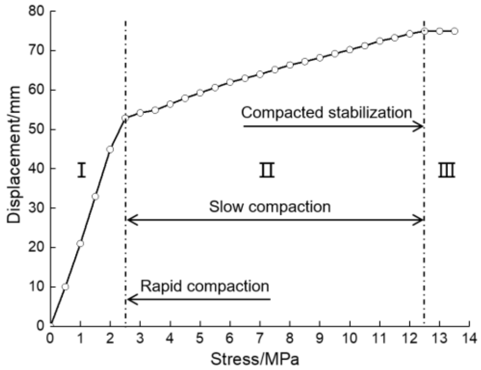

(a) Stress-displacement curve

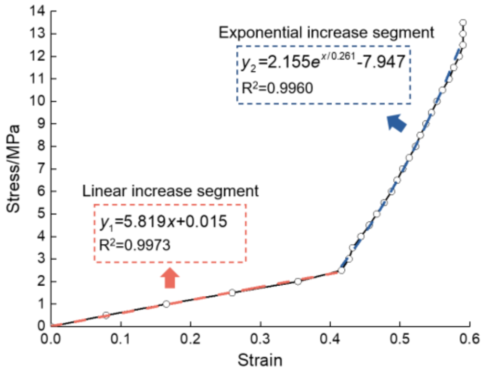

(b) Stress-strain curve

Fig.16 Experiment results

The compression displacement was 75 mm.

Fig. 16 shows the experimental results with regard to stress-strain and stress-displacement characteristics of the bulking limestone gravel. As shown in Fig. 16(a), the three stages of rapid compaction, slow compaction, and compacted stabilization can be identified, which is identical to the stress-displacement characteristics in Section 4.3. The deformation in stage I accounted for 70.5% of the total displacement, corresponding to the result of ~70% in Section 4.3. In addition, the stress reached 2.5 MPa at the end of stage I, which is 18.5% of the compressive strength of the limestone. This result is likely close to the one-sixth reported in Section 4.3.

Meanwhile, Fig. 16(b) shows the stress-strain curve when the limestone gravel was compacted. Similarly, the curve increased linearly and then went up exponentially. The fitting results showed R^2=0.9973 in the linear increase segment while using the linear function, and R^2=0.9960 in the exponential increase segment while using the natural exponential function. This increasing trend is the same as the trend shown in Section 4.4.

Therefore, although there may be differences in the absolute value, the trend is consistent while using the well-prepared gypsum samples to simulate the bulking rock mass. The value differences were mainly due to the variation in strength between the limestone and the gypsum.

(a) Initial state

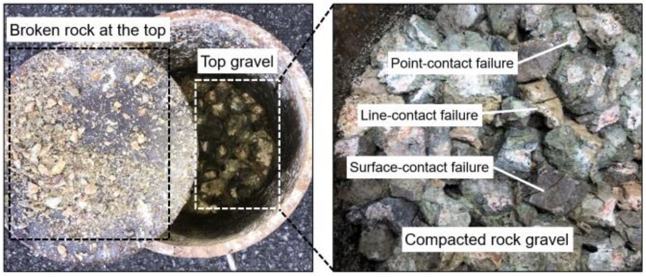

(b) Compacted state

Fig. 17 Compaction failure characteristics of the limestone gravel

Fig. 17 shows the characteristics of the limestone gravel before and after the compaction. Fig. 17(a) shows that the irregular rock gravel was randomly stacked. After the compaction, the bulking rock was severely broken at the top, as shown in Fig. 17(b). This failure characteristic was consistent with the result in Section 4.4. Observing the top gravel after the compaction, we could find the three failure forms of the point-, line-, and surface-contact failure, corresponding to the results in Section 4.4. In addition, the space ratio was in the range of 0.15–0.2 in this experiment. We could obtain K_I=1.89 and K_R=1.30 based on the experiment data. According to Table 7, when the space ratio was 0.15–0.2, the average K_I and K_R were 2.31 and 1.30. Therefore, the K_R was the same. The difference in K_I was mainly due to the shape of objects. The limestone was rugged and irregular while the gypsum sample was regularly cubic. The sharp-edged samples would result in a higher K_I, so the K_I of the gypsum sample was bigger than that of limestone. However, the K_R was the same because of the similar trend during the compaction. Therefore, although some absolute values differed, the overall pattern was consistent during compaction. Because the gypsum was easily molded, this advantage helps block out many distractions so that we can focus on the SSE effect of broken-expansion rock mass. The above comparisons demonstrate the rationality and present limitations of replacing rock gravel with gypsum sample in this study.

5.2 Implications to 110/N00 mining method

The 110/N00 mining method utilizes the volume increase effect caused by broken-expansion mass to achieve mining compensation (He *et al.* 2021). A generalized formula yields the desired broken-expansion volume ΔV_B:

$$\Delta V_B=(K-1)H_C A \tag{6}$$

where K is the broken-expansion factor, H_C is the roof-cutting height, and A is the mining area.

Therefore, if in a specific site, we should adjust the cutting height H_C to achieve a desired volume ΔV_B, and the broken-expansion factor K and the mining area A possibly vary significantly in different sites. First, according to the results in Sections 4.1 and 4.2, the factors K_I and K_R increased as the block size L and the space ratio S increased, and the broken-expansion factors increased more evidently when the accumulation area M increased. These rules suggest that having a larger mining area is advantageous for implementing the 110/N00 mining method. This would allow us to lower the height of the roof cutting. While a larger accumulation area may result in greater effects of broken-expansion factors, observations in Section 4.4 indicate that the compressive capacity of the bulking mass is better during compaction in a smaller accumulation area. In this case, the support effect of the broken-expansion mass is more prominent.

In addition, Section 4.4 states that when the upper samples fail, they fill voids in the lower samples while the lower samples adjust their positions to prevent failure. This phenomenon tells that the compressive strength of the caved upper strata within the mass is important for supporting the bulking mass. When the broken-expansion mass is compressed under the mining pressure, its compressive capacity can increase exponentially, as shown in Section 4.4. These results confirm the natural support effect of the broken-expansion mass. Therefore, it is feasible that the 110/N00 mining method utilizes the broken-expansion effect of caved roof to mitigate the mining pressure from strata movement.

6. Conclusions

The broken-expansion mass performs a crucial role in the 110/N00 mining method. This work employed the rock-like material to study the spatial size effect (SSE) of broken-expansion mass via laboratory tests. The space ratio S and SEE coefficient C were first defined to quantify and characterize the SSE. We then examined the SSE on the initial (K_I) and residual (K_R) broken-expansion factors. Both the factors increase as the sample size and the space ratio increase, and this increase can be enlarged while the sample size and the space ratio become great. Compared to the sample size, the space ratio is better for observing the SSE of the broken-expansion factors. The space ratio of 0.2 is the turning point where the factors start to increase rapidly in this study. A larger accumulation area can lead to a more evident increase effect. Generally, K_I determines K_R in terms of SSE, but the compression shows an inhibition to SSE. The inhibition is more noticeable when the sample size and the accumulation area become larger. The SSE coefficient C helps explain the inhibition because C_R reduces from C_I. The SSE coefficient C also describes the SSE variation trend well as the sample size increases.

Based on the SSE of the broken-expansion factors, we observed the displacement, mechanical, and failure characteristics of bulking samples during their compactions. First, the SSE of displacement characteristics is distinct. The SSE coefficient can express the difference in displacement characteristics between sample sizes. When the difference between C_I and C_R is significant, the displacement differentiation by different sample sizes clearly exists, and the change of space ratio contributes too. Additionally, there are three stages involved in the compaction process: rapid compaction, slow compaction, and compacted stabilization. During the rapid compaction, one-sixth of the material's compressive strength is responsible for around 70% of the total displacement. The remaining five-sixths of the strength causes the rest 30% displacement in the slow compaction stage. If a larger space ratio is used, more vertical space can be created, leading to a more significant reduction in volume.

Furthermore, the stress-strain curves indicate that a linear increase segment corresponds to the rapid compaction stage, followed by an exponential increase in the latter two stages. The broken-expansion mass shows a growing compressive capacity during the compaction, which can benefit from a smaller accumulation area. The point-, line-, and surface-contact failures are observed during the compression. The compression failure is essentially a dynamic process, in which the point and line contacts are transformed into the surface contacts, and the structure is changed from loose into firm. The upper samples fail and then fill voids while the lower samples spontaneously adjust their positions to prevent failure. Eventually, the bulking samples are compacted into a high-strength body resistant to compression.

Finally, we compare and analyze the results of the tests conducted on gypsum and limestone gravel samples. Both samples have similar compaction trends and characteristics, including compression displacement, mechanical, and failure characteristics. Although there may be differences in the absolute values due to the different strengths and shapes, the overall trends remain consistent. Meanwhile, the gypsum sample has the advantage of easy molding to facilitate studying the SSE effect of broken-expansion rock mass

Acknowledgments

This work was supported by the National Natural Science Foundation of China (No. 51904188) and the Key Laboratory of Rock Mechanics and Geohazards of Zhejiang Province (No. ZJRMG-2022-03), which are gratefully acknowledged.

References

Bednarek, L. and Majcherczyk, T. (2020), "An analysis of rock mass characteristics which influence the choice of support", *Geomech. Eng.*, **21**(4), 371-377. https://doi.org/10.12989/gae.2020.21.4.371.

Chang, L., Konietzky, H. and Frühwirt, T. (2019), "Strength anisotropy of rock with crossing joints: Results of physical and numerical modeling with gypsum models", *Rock Mech. Rock Eng.*, **52**, 2293-2317. https://doi.org/10.1007/s00603-018-1714-8

Das, S.K. (2000), "Observations and classification of roof strata behaviour over longwall coal mining panels in India", *Int. J. Rock Mech. Min. Sci.*, **37**(4), 585-597.

Discenza, M.E., Martino, S., Bretschneider, A. and Scarascia

Mugnozza, G. (2020), "Influence of joints on creep processes involving rock masses: results from physical-analogue laboratory tests", *Int. J. Rock Mech. Min. Sci.*, **128**. https://doi.org/10.1016/j.ijrmms.2020.104261.

Fairhurst, C. (2017), "Some challenges of deep mining. engineering", **3**(4), 527-537. https://doi.org/10.1016/J.Eng.2017.04.017.

Fakhimi, A. and Tarokh, A. (2013), "Process zone and size effect in fracture testing of rock", *Int. J. Rock Mech. Min. Sci.*, **60**, 95-102. https://doi.org/10.1016/j.ijrmms.2012.12.044.

Fan, L. and Liu, S. (2017), "A conceptual model to characterize and model compaction behavior and permeability evolution of broken rock mass in coal mine gobs", *Int. J. Coal Geol.*, **172**, 60-70. https://doi.org/10.1016/j.coal.2017.01.017.

Fu, Q., Yang, J., Gao, Y., Li, C., Song, H., Liu, Y. and Wu, X. (2024), "Combined blasting for protection of gob-side roadway with thick and hard roof", *J. Rock Mech. Geotech. Eng.*, **16**(8), 3165-3180. https://doi.org/10.1016/j.jrmge.2023.11.027.

Gell, E.M., Walley, S.M. and Braithwaite, C.H. (2019), "Review of the validity of the use of artificial specimens for characterizing the mechanical properties of rocks", *Rock Mech. Rock Eng.*, **52**, 2949-2961. https://doi.org/ 10.1007/s00603-019-01787-8.

Genis, M., Akcin, H., Aydan, O. and Bacak, G. (2018), "Investigation of possible causes of sinkhole incident at the Zonguldak Coal Basin, Turkey", *Geomech. Eng.,* **16**(2), 177-185. https://doi.org/10.12989/gae.2018.16.2.177.

Guo, P., Liang, H., Zhang X., Liu, X., Jin. Z. and Ye, K. (2024), "A new method of cutting seam for preventing strain rock burst: Insights from experimental and numerical tests", *Rock Mech. Rock Eng.*, **57**(11), 9923-9939. https://doi.org/10.1007/s00603-024-04073-4

Guo, Z., Wang, Q., Yan, D., Li, M., Yin, S. and Qu, Y. (2019), "The creep compaction behavior of crushed mudstones under the step loading in underground mining", *Int. J. Coal Sci. Technol.*, **6**(3), 408-418. https://doi.org/10.1007/s40789-019-0243-8.

Haftani, M., Bohloli, B., Nouri, A., Maleki Javan, M.R. and Moosavi, M. (2014), "Size effect in strength assessment by indentation testing on rock fragments", *Int. J. Rock Mech. Min. Sci.*, **65**, 141-148. https://doi.org/10.1016/j.ijrmms.2013.10.001.

Haeri, H., Sarfarazi, V., Shemirani, A.B. and Hosseini, S.S. (2017), "Experimental and numerical investigation of the effect of sample shapes on point load index", *Geomech. Eng.*, **13**(6), 1045-1055. https://doi.org/10.12989/gae.2017.13.6.1045.

He, M., Wang, Q. and Wu, Q. (2021), "Innovation and future of mining rock mechanics", *J. Rock Mech. Geotech. Eng.*, **13**(1), 1-21.

Lee, G., Ryu, H., Cho, G. and Kwon, T. (2023), "Full-scale TBM excavation tests for rock-like materials with different uniaxial compressive strength", *Geomech. Eng.*, **35**(5), 487-497. https://doi.org/10.12989/gae.2023.35.5.487.

Li, J., Huang, Y., Pu, H., Gao, H., Li, Y., Ouyang, S. and Guo, Y. (2021), "Influence of block shape on macroscopic deformation response and meso-fabric evolution of crushed gangue under the triaxial compression", *Powder Technol.*, **384**, 112-124. https://doi.org/10.1016/j.powtec.2021.02.001.

Liu, H., Zhao, Y., Ren, T., Wang, F. and Li, Z. (2022), "Characteristics of overburden failure and fracture development in gob of mining with gob-side entry formed by cutting roof", *J. China University Min. Technol.*, **51**(1), 78-89.

Liu, J., He, M., Hou, S., Zhu, Z., Wang, Y. and Yang, J. (2021), "Force change of the gravel side support during gangue heaping under a new non-pillar-mining approach", *Geomech. Eng., 27*(1), 31-43. https://doi.org/10.12989/gae.2021.27.1.031.

Liu, J., He, M., Ming, C., Zhang, J., Yang, G., Guo, L., Guo, S., Rodriguez-Dono, A. and Zhu, Z. (2022), "Study on the bearing characteristics of random lumpiness gangue from a gob roof", *Bull. Eng. Geol. Environ.*, **81**(10). https://doi.org/10.1007/s10064-022-02927-1.

Ma, D., Duan, H., Liu, J., Li, X. and Zhou, Z. (2019), "The role of gangue on the mitigation of mining-induced hazards and environmental pollution: An experimental investigation", *Sci. Total Environ.*, **664**, 436-448. https://doi.org/10.1016/j.scitotenv.2019.02.059.

Meng, F., Pu, H., Sasaoka, T., Shimada, H., Liu, S., K.M Dintwe, T. and Sha, Z. (2021), "Time effect and prediction of broken rock bulking coefficient on the base of particle discrete element method", *Int. J. Min. Sci. Technol.*, **31**(4), 643-651. https://doi.org/10.1016/j.ijmst.2021.05.004.

Moghaddam, R. and Golshani, A. (2024), "Experimental study on fracture propagation in anisotropy rock under cyclic hydraulic fracturing", *Eng. Fract. Mech.,* **295**. https://doi.org/10.1016/j.engfracmech.2023.109775.

Moosavi, M. and Ghadernejad, S. (2021), "A novel method for predicting the swelling potential of clay-bearing rocks", *Geomech. Eng.*, **27**(6), 615-626. https://doi.org/10.12989/gae.2021.27.6.615.

Pour, A., Afrazi, M. and Golshani, A. (2022), "Experimental study of the effect of length and angle of cross-cracks on tensile strength of rock-like material", *Iran. J. Sci. Technol. Trans. Civ. Eng.,* **46**:4543-4556 https://doi.org/10.1007/s40996-022-00891-0.

Sarfarazi, V., Asgari, K. and Nasrollahi, M. (2021), "Interaction between rock bolt and rock bridge under tensile loading", *Geomech. Eng.*, **25**(6), 455-471. https://doi.org/10.12989/gae.2021.25.6.455.

Wang, J. (2014), "Development and prospect on fully mechanized mining in Chinese coal mines", *Int. J. Coal Sci. Technol.*, **1**(3), 253-260. https://doi.org/10.1007/s40789-014-0017-2.

Wang, Q., Guo, Z., Zhu, C., Yin, S. and Yin, D. (2021). "The deformation characteristics and lateral stress of roadside crushed rocks with different particles in non-pillar coal mining", *Energies*, **14**(13). https://doi.org/10.3390/en14133762.

Yang, L., Yang, A., Chen, S., Fang, S., Huang, C. and Xie, H. (2021). "Model experimental study on the effects of in situ stresses on pre-splitting blasting damage and strain development", *Int. J. Rock Mech. Min. Sci.*, **138**. https://doi.org/10.1016/j.ijrmms.2020.104587.

Yavuz, H. (2004), "An estimation method for cover pressure re-establishment distance and pressure distribution in the goaf of longwall coal mines", *Int. J. Rock Mech. Min. Sci.*, **41**(2), 193-205. https://doi.org/10.1016/s1365-1609(03)00082-0.

Zhang, X., Chen, L., Gao, Y., Hu, J., Yang, J. and He, M. (2019), "Study of an innovative approach of roof presplitting for gob-side entry retaining in longwall coal mining", *Energies*, **12**(17). https://doi.org/10.3390/en12173316.

Zhang, X., He, M., Yang, J., Wang, E., Zhang, J. and Sun, Y. (2020), "An innovative non-pillar coal-mining technology with automatically formed entry: a case study", *Engineering*, **6**(11), 1315-1329. https://doi.org/10.1016/j.eng.2020.01.014.

Zhang, X., Pak, R. Y. S., Gao, Y., Liu, C., Zhang, C., Yang, J. and He, M. (2020), "Field experiment on directional roof presplitting for pressure relief of retained roadways", *Int. J. Rock Mech. Min. Sci.*, **134**. https://doi.org/10.1016/j.ijrmms.2020.104436.

Zhang, X., Pak, R. Y. S., Yang, J., Lei, L., Niu, H., Niu, Y., Zhao, C. and Gao, H. and He, M. (2023), "Mechanistic formulation and validation of cutting seam by energy-focusing blast for pressure relief of deep roadway", *Eng. Fail. Anal.*, **150**. https://doi.org/10.1016/j.engfailanal.2023.107378.

GC